Journal of Ship Research, Vol. 51, No. 1, March 2007, pp. 1–21

Journal of
Ship Research

An Experimental Investigation Into the Performance of a Flush Water-Jet Inlet

P. A. Brandner* and **G. J. Walker†**

**Faculty of Maritime Engineering, Australian Maritime College, Launceston, Tasmania, Australia*
†*School of Engineering, University of Tasmania, Hobart, Tasmania, Australia*

An experimental investigation of the flow within a generic flush type water-jet inlet has been carried out to identify the principal flow features and provide a basis for development of computational fluid dynamics (CFD) models. Tests were performed in a cavitation tunnel with the model inlet fitted to the test section ceiling, and effects of thickening the ingested tunnel wall boundary layer were investigated. The model was fitted with a range of instrumentation to investigate the ramp pressure distribution and boundary layer development, lip incidence, and pump face flow properties. Observations of lip and duct cavitation inception and behavior were also made. The results showed the inlet performance to be generally improved with the ingestion of a thicker boundary layer. The thickened boundary layer significantly reduced ramp boundary layer separation and distortion of flow at the notional pump face. However, a greater range of lip incidence occurred with the thickened boundary layer with consequent greater likelihood of lip separation and cavitation occurrence. Ideal lip incidence and pump face flow uniformity occurred at flow parameters significantly different from those for ideal pump face pressure recovery. Large developed cavities on the inlet lip were observed for a range of conditions typical of conventional high-speed vessel operation.

1. Introduction

WATER JETS with flush type inlets are almost universally used for propulsion of large high-speed craft (Fast Ferry International 2001). They overcome many problems that would be associated with open propulsors, such as achievable energy densities, the presence of exposed mounting brackets, and cavitation. Advances in computational fluid dynamics (CFD) and experiment have accelerated the development of inlets for application to large high-speed ships, but flush inlets remain a relatively recent development (for large fast ferries developed in the late 1980s and 1990s) and there is limited information on inlet flow behavior, at least in the open literature. A significant review and investigation of early work on the performance of water-jet propulsors is given by Allison (1993). Roberts (1998) later presented extensive wind tunnel investigations of flush inlet performance and a further detailed review. Seil (1998) carried out detailed CFD investigations of flush inlet performance and optimization of duct geometry. The several RINA conference proceedings (1994, 1998, 2000, and 2004) provide additional reviews and detail the latest developments.

Significant aspects of water-jet inlet flow include hull boundary layer ingestion, an S-shaped duct geometry, diffusion of the bulk flow, variation of the inlet streamtube shape with the inlet velocity ratio (IVR), and the presence of the pump rotor shaft in the flow path. The vessel hull boundary layer thickness is typically similar to the nominal inlet duct size; this is a major factor in flow development within the duct and increases the possibility of ramp flow separation and distortion of the pump face velocity distribution. This is a major point of difference from aero-engine inlet flow, where the fuselage boundary layers are relatively much thinner and often diverted from the inlet altogether. While boundary layer ingestion may exacerbate flow problems, its diversion in marine inlets would seem impractical, and boundary layer ingestion is in any case advantageous in terms of overall propulsive efficiency. The S-shaped nature of the inlet duct introduces secondary flows where both viscous and pressure field effects have an

Manuscript received at SNAME headquarters March 3, 2005; revised manuscript received October 4, 2005.

influence. The hull boundary layer, as well as internal and external corners of the inlet duct and ramp walls, further complicate the secondary flows. The requirement for a diffusing (flow decelerating) duct introduces adverse (positive) pressure gradients within the inlet ducting that coupled with low-energy hull boundary layer fluid may lead to flow separation within the inlet duct. Adverse pressure gradients and flow separation may also be induced by longitudinal curvature effects. The variation of inlet streamtube shape with IVR causes changes in lip incidence that influence cavitation onset, with lip cavitation more likely to occur at off-design conditions, such as maneuvering or light ship cruise. The wake of the rotor shaft exacerbates the problem of low-energy fluid, as it combines with the region of stalled flow at the top of the duct to produce a major local distortion of the pump face velocity distribution.

Given the complex three-dimensional nature of inlet flow, CFD offers great opportunity for optimization in inlet duct design, as illustrated by Seil (1998). However, experimental data are still required for development and validation of CFD modeling as well as for basic flow investigations. For this purpose, a water-jet inlet test loop was developed as part of the Australian Maritime College (AMC) cavitation tunnel, as described by Brandner and Walker (2001). A range of instrumentation has been specifically designed to investigate the flow phenomena in this facility. The present paper describes extensive measurements of flow in a generic flush inlet that provide insight into basic phenomena and provide valuable quantitative data for CFD comparisons.

2. Experimental overview

2.1. Water-jet inlet model

The geometry of the inlet model used for the present investigation is that developed for wind tunnel tests by Roberts (1998), although a dummy, nonrotating, pump rotor shaft has been added. This generic geometry may be considered typical of a conventional flush inlet design. The entrance ducting consists of a semicircular lower half and a rectangular section upper half with 22.5 deg ramp angle transitioning to a circular duct with a lobster back bend ahead of a 150 mm diameter straight duct connecting the pump. Full details of the duct geometry and dummy shaft are shown in Fig. 1. The model scale is nominally 1:10 based on duct sizes typically used on 75 m to 100 m high-speed ships.

2.2. Experimental setup

All tests were performed in the AMC Tom Fink Cavitation Tunnel, a closed-circuit variable-pressure water tunnel. The test section is 0.6 m × 0.6 m in cross section by 2.6 m long. The velocity may be varied from 2 to 12 m/s and the centerline static pressure from 4 to 400 kPa absolute. Studies may involve the investigation of steady and unsteady flows, two-phase flows including cavitation, turbulence, and hydroacoustics. Basic details of the cavitation tunnel and water-jet test loop are given in Appendix B. Full details of the tunnel and water-jet inlet test loop are given in Brandner and Walker (2001).

The inlet model was fitted to the ceiling of the test section, as shown in Fig. 2. A general view of the installation is shown in Fig. 3. Tests were performed with both the natural test section wall boundary layer and an artificially thickened boundary layer. The thickener was a saw-toothed fence chosen from a range of devices tested by Brandner and Walker (2001) as being the most efficient, having the lowest inception cavitation number; its location is shown in Fig. 2. This thickener has since been used in many studies in the cavitation tunnel and has also been investigated in detail in wind tunnel tests by Sargison et al. (2004). The thickener produces a nominal 50 mm thick boundary layer at the reference position shown in Fig. 2, with velocity and turbulence distribu-

Nomenclature

A = duct cross-sectional area

A_J = nominal inlet area = $\frac{\pi D_J^2}{4}$

$C_{p\infty}$ = static pressure coefficient = $\frac{p - p_\infty}{\frac{1}{2}\rho U_\infty^2}$ (based on freestream dynamic pressure)

C_{pJ} = static pressure coefficient = $\frac{p - p_\infty}{\frac{1}{2}\rho U_J^2} = \mathrm{IVR}^2 C_{p\infty}$ (based on dynamic pressure corresponding to mean exit velocity)

ASPC = circumferential averaged static pressure coefficient = $\frac{\int_{Circ} C_p dl}{\int_{Circ} dl}$

C_P = total pressure coefficient = $\frac{P - p_\infty}{\frac{1}{2}\rho U_\infty^2}$

AATPC = area averaged total pressure coefficient = $\frac{\int_{\mathrm{AREA}} C_P dA}{\int_{\mathrm{AREA}} dA}$

AATPC_{60} = lowest area averaged total pressure coefficient over a 60 deg sector

FATPC = flow averaged total pressure coefficient = $\frac{\int_{\mathrm{AREA}} C_P u dA}{\int_{\mathrm{AREA}} u dA}$

D_J = duct diameter at notional pump face

DC_{60} = distortion coefficient = $(\mathrm{AATPC} - \mathrm{AATPC}_{60})\mathrm{IVR}^2$

I = circumferential distance

IVR = inlet velocity ratio = $\frac{U_\infty}{U_J}$

p = static pressure

p_v = vapor pressure

p_∞ = freestream static pressure

$p_{\infty L}$ = freestream static pressure at lip elevation

P = total pressure = $p + \frac{1}{2}\rho U^2$

Q_J = water-jet volumetric flow rate

r = radius

$R_{n\infty}$ = Reynolds number = $\frac{D_J U_\infty}{\nu}$ (based on freestream velocity)

R_{nJ} = Reynolds number = $\frac{D_J U_J}{\nu} = \frac{R_{n\infty}}{\mathrm{IVR}}$ (based on mean exit velocity)

U = local velocity

U_J = mean exit velocity = $\frac{Q_J}{A_J}$

U_∞ = freestream velocity

$\frac{u}{U_J}$ = velocity ratio = $\mathrm{IVR}\sqrt{C_P - C_p}$

u = axial velocity (relative to local duct centerline)

v = tangential velocity (relative to local duct centerline)

x = surface arc length on duct center plane

y = ordinate normal to local surface direction

ρ = fluid density

α = swirl angle of absolute flow = $\arctan\frac{v}{u}$

ν = kinematic viscosity

σ_∞ = cavitation number = $\frac{p_{\infty L} - p_v}{\frac{1}{2}\rho U_\infty^2}$ (based on freestream dynamic pressure)

σ_J = cavitation number = $\frac{p_{\infty L} - p_v}{\frac{1}{2}\rho U_J^2} = \mathrm{IVR}^2\sigma_\infty$ (based on dynamic pressure corresponding to mean exit velocity)

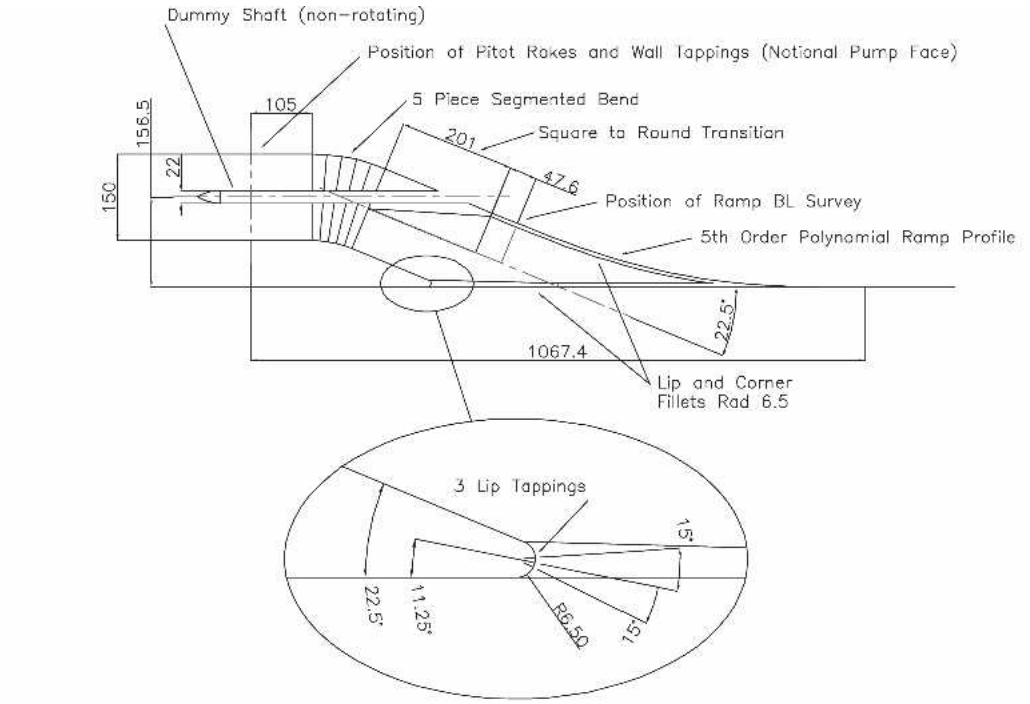

(a) Model Inlet Dimensions on Vertical Centerline

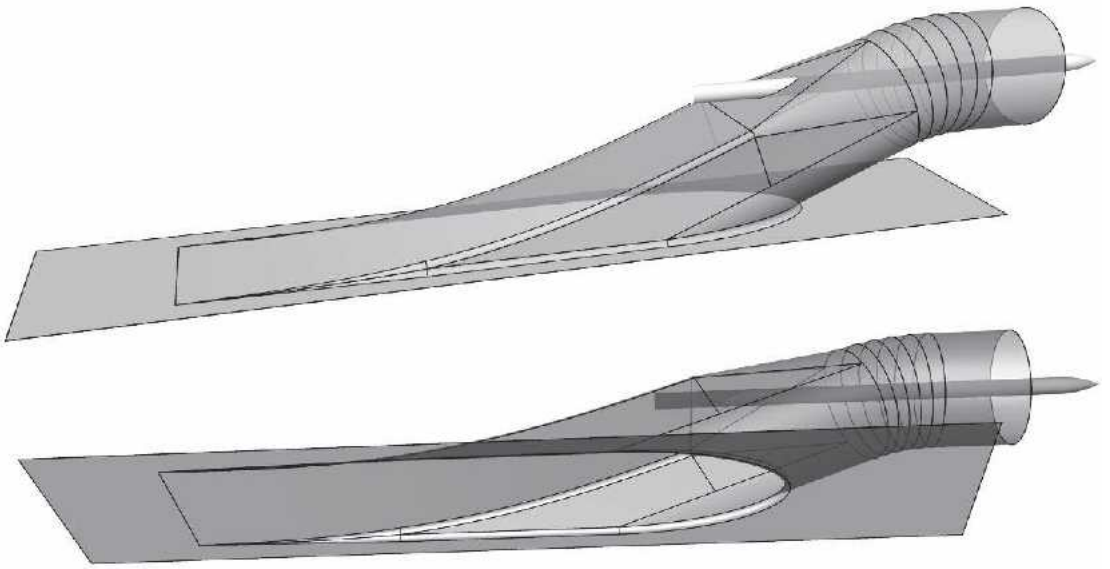

(b) Model Inlet 3-Dimensional View

Fig. 1 Model inlet duct geometry (dimensions in millimeters)

tions closely matching those of an equilibrium flat plate turbulent boundary layer (Brandner et al. 2004). A correct turbulence distribution as well as a velocity distribution is vital for correct modeling of viscous flow within the inlet duct. The natural boundary layer thickness at the reference position is 20 mm, with properties that very closely match those of an equilibrium flat plate turbulent boundary layer.

The model is fitted with a range of instrumentation developed to investigate the principal features of the inlet flow, including ramp pressure distribution and boundary layer development, lip incidence, and pressure and velocity distributions at the pump face. The model is fitted with 17 wall tappings on the centerline of the ramp and upper half of the duct to measure the longitudinal distribution of static pressure over the entire inlet length. A mounting gland at the position shown in Fig. 2 permits the insertion of pressure probes to survey the ramp boundary layer and flow pro-

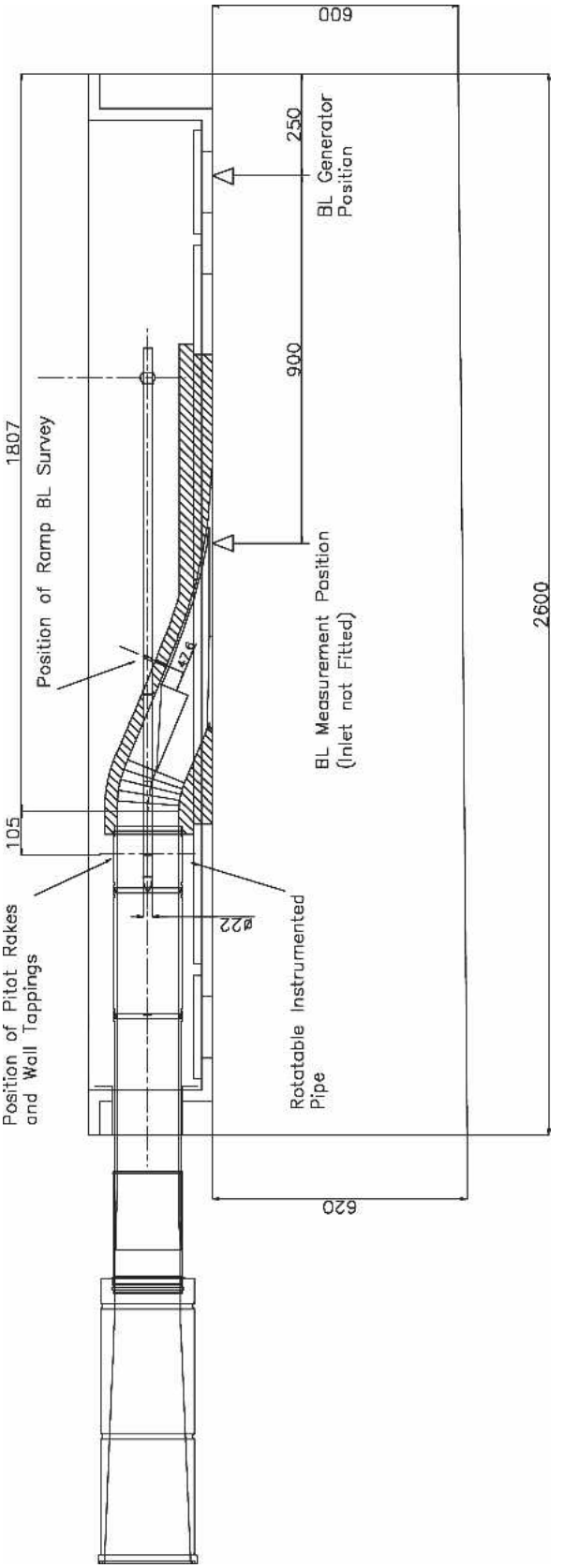

Fig. 2 Location of model inlet, instrumentation, and boundary layer thickener in tunnel test section (dimensions in millimeters; test section width = 600 mm)

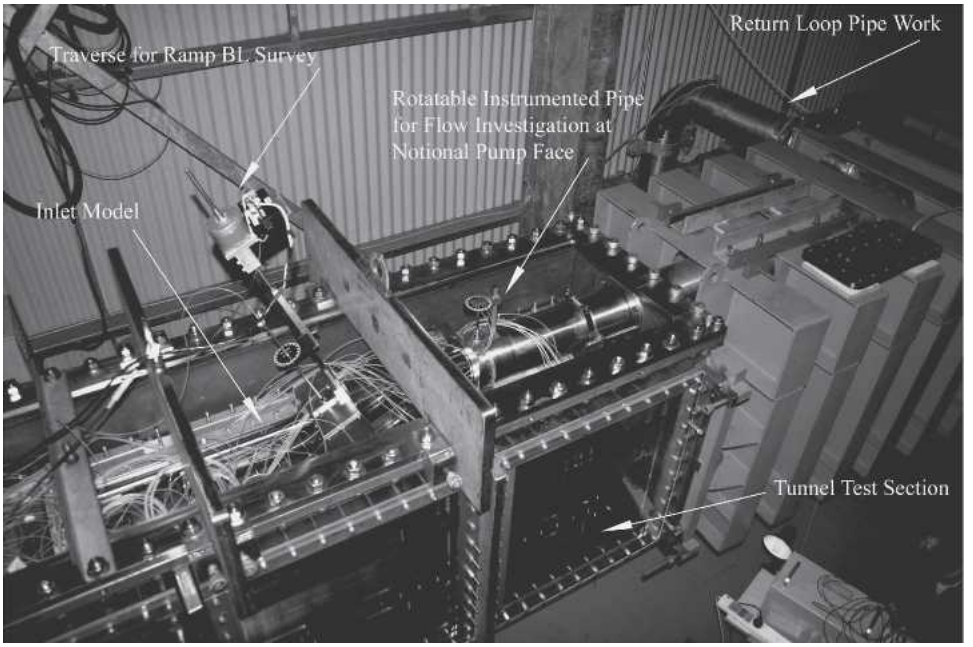

Fig. 3 View of experimental test setup

files just upstream of the shaft entrance. These boundary layer profiles were measured using a 1.6 mm diameter total head tube and wall static tap in the plane of the tube tip. The probe was positioned using a computer-controlled traverse with an estimated precision of better than 0.01 mm. The intake lip has three 1 mm diameter pressure tappings on the inlet vertical center plane: one on the bisector of the lip, and two others 15 deg above and below on the circular arc lip profile. These pressure measurements permit the determination of lip incidence and indicate whether the stagnation streamline originates from the freestream or from within the approaching boundary layer.

An instrumented pipe length is fitted downstream of the inlet to investigate flow properties at the notional pump face, where the duct diameter is 150 mm. This pipe length is rotatable and may be configured for fixed Pitot rakes or a traversing three-hole cobra probe. The Pitot rake comprises two rakes 180 deg apart, each with five 1.6 mm diameter total head tubes. The total head tubes are distributed with greater density toward the duct wall to best capture the flow profile. On one half of the periphery between the Pitot rake locations there are eight wall pressure tappings spaced at 20 deg intervals. A three-hole pressure probe (2.5 mm nominal head size) is used in combination with the total head rakes to measure the axial and tangential velocity components that are generally of most interest from the viewpoint of pump operation. This provides an economic means of studying secondary flows without the expense of calibrating and using a five-hole pressure probe (although subject to error in regions of significant radial flow). The three-hole probe configuration has a traverse to allow measurements at arbitrary radial positions, although the present measurements were made at the same positions as the total head tubes in the rakes. The three-hole probe was traversed across the full diameter through a hole in the shaft, as the pipe could not be rotated through the full 360 deg due to interference of the probe support with the tunnel wall. The three-hole probe was calibrated at six Reynolds numbers and ±24 deg yaw against a Pitot static tube. All pressures (as well as tunnel instrument pressures) were sequentially measured relative to the tunnel static pressure using a Validyne Model DP15TL differential pressure transducer via a Model 48J7-1 Scanivalve pressure multiplexer.

Parameters measured during testing include tunnel pressure, velocity, temperature, and dissolved oxygen content. Online instrumentation is used for automatic control of tunnel pressure and velocity as well as real time data monitoring and acquisition. The test section pressure is measured using two Rosemount Model 3051C Smart absolute pressure transducers in parallel. Test section velocity is derived from the contraction pressure differential measured using two Rosemount Model 1151 Smart differential pressure transducers in parallel. One of each pressure transducer pair has a lower range to improve measurement precision at lower pressures and velocities, respectively. The estimated precision of the absolute pressure measurement is 0.1 kPa for pressures up to 120 kPa and 0.5 kPa for pressures up to 400 kPa. The estimated precision of the velocity measurement is 0.05 m/s. Water temperature is measured to 0.5 deg C accuracy using a Rosemount Model 244 temperature transducer. Dissolved oxygen content is measured using a Rosemount Model 499 dissolved oxygen sensor. Water-jet loop flow rate was measured using a 200 NB ABB Process Magmaster electromagnetic flow meter with an estimated precision of ±0.2%.

2.3. Experimental procedure

The following tests were performed:

- Measurement of ramp boundary layer profiles
- Measurement of ramp/duct upper centerline pressure distribution
- Measurement of lip pressures and incidences
- Measurement of pump face flow parameters
- Observation of lip/duct cavitation inception and occurrence.

Ramp boundary layer profiles were measured with both natural and thickened test section boundary layers at $R_{n\infty} = 1 \times 10^6$ and IVR values of 1.0, 1.25, 1.5, 1.75, and 2.0. Each profile typically comprised 50 measurement points with spacing varied logarithmically from 0.1 mm adjacent to the wall to 10 mm at the outer edge of the boundary layer. Ramp/duct upper centerline surface pressure distributions were measured with both natural and thickened test section boundary layers at $R_{n\infty} = 1 \times 10^6$ and IVR values of 0.75, 1.0, 1.25, 1.5, 1.75, 2.0, 2.5, and 3.0. To investigate Reynolds number effects, measurements were also made at $R_{n\infty} = 0.5 \times 10^6$, 0.75×10^6, 1.0×10^6, 1.25×10^6, and 1.5×10^6 at an IVR of 1.75.

Lip pressures were measured with both natural and thickened test section boundary layers at $R_{n\infty} = 1 \times 10^6$ and IVR values of 0.0, 0.25, 0.5, 0.75, 1.0, 1.25, 1.5, 1.75, 2.0, 2.5, and 3.0. To investigate Reynolds number effects, measurements were also made at $R_{n\infty} = 0.5 \times 10^6$, 0.75×10^6, 1.0×10^6, 1.25×10^6, and 1.5×10^6, at IVR values of 1.0, 1.25, 1.5, 1.75, and 2.0.

Pump face total pressure and derived velocity distributions were obtained with both natural and thickened test section boundary layers at $R_{n\infty} = 1 \times 10^6$ and IVR values of 1.0, 1.25, 1.5, 1.75, and 2.0. Reynolds number variation was found to have only a small effect on the distribution of total pressure and was not investigated in any further detail. Pump face swirl distributions were measured with both natural and thickened test section boundary layers at $R_{n\infty} = 1 \times 10^6$ and IVR values of 1.5, 1.75, and 2.0 with the thickened boundary layer, and an IVR value of 1.75 only with the natural boundary layer. The pressure data from all transducers were acquired at 300 Hz and averaged over 10 seconds. Pressure transducer zero errors were minimized by observing the zero readings on each pressure scan. The contraction differential was also monitored on each scan and was used to nondimensionalize measured pressures to eliminate pressure transducer span error. Acquired data were corrected for small temporal changes using the tunnel contraction differential during postprocessing. The effects of tunnel blockage may be investigated in detail using CFD, as performed by Verbeek and Bulten (2001), although for the purposes of the present study all measured pressures are adjusted for tunnel blockage using a one-dimensional analysis detailed in Appendix A.

All cavitation observations were nominally made at $R_{n\infty} = 1 \times 10^6$ for IVR values greater than 1 and at R_{nJ} values of 0.85×10^6, 0.75×10^6, 0.5×10^6, and 0.25×10^6 for IVR values less than 1. For cavitation observations, the tunnel water dissolved gas content was maintained at approximately 30% of saturation at atmospheric pressure. Cavitation inception in steady flow was defined as occurring when cavities were first observed to appear visually using stroboscopic lighting, or if intermittent when these were present for 50% of the time.

3. Results

3.1. Ramp boundary layer

Figures 4 and 5 show the measured boundary layer profiles upstream of the inlet and within the duct for natural and thickened boundary layers, respectively. The ramp boundary layer fluid is seen to undergo a greater deceleration in the natural boundary layer case compared with that of the thickened boundary layer. For IVR values greater than 1.5, flow separations occur for the natural boundary layer case, whereas separation never occurs over the IVR range tested with the thickened boundary layer. The ramp boundary layer experiences a slightly more adverse pressure gra-

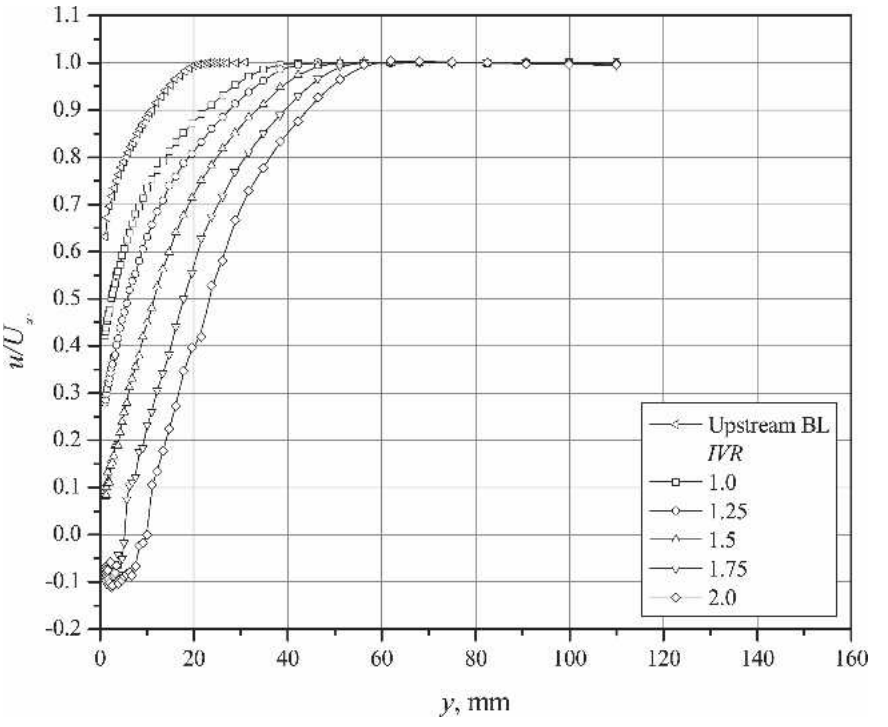

Fig. 4 Ramp boundary layer velocity profiles with natural wall boundary layer (measured just upstream of shaft penetration)

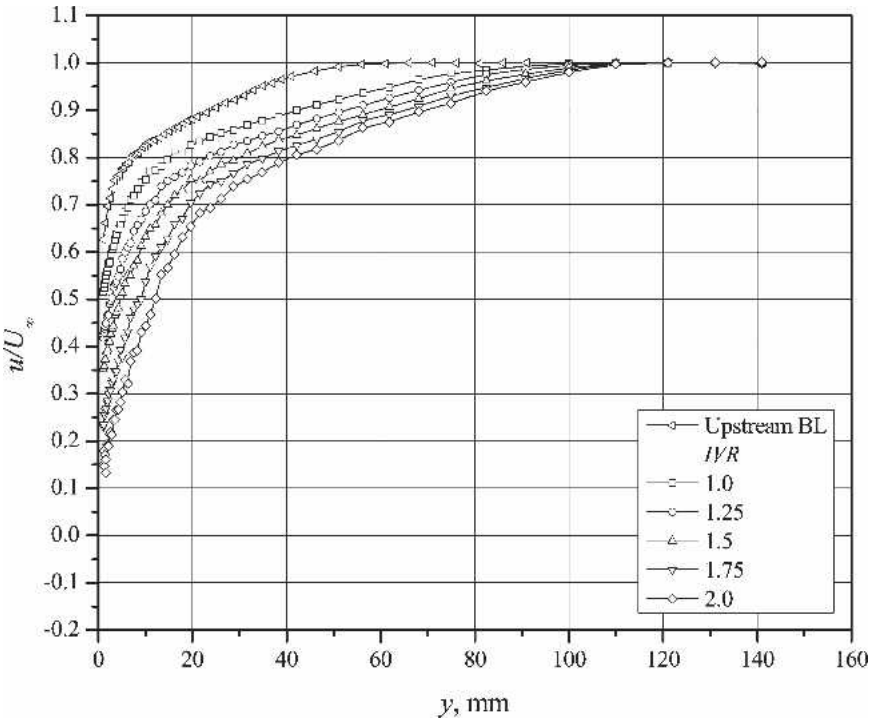

Fig. 5 Ramp boundary layer velocity profiles with thickened wall boundary layer (measured just upstream of shaft penetration)

dient for the natural inlet boundary layer case, as discussed below. Evidently for the thicker boundary layer, divergence of flow on the ramp due to secondary flows and the effects of reduced longitudinal pressure gradient more than compensate for the greater inlet boundary layer thickness. Although the flow in the duct is complicated by transverse pressure gradients and secondary flows, the ramp pressure gradient is the fundamental parameter controlling ramp separation.

The measured centerline velocity profile, combined with simple flow visualization using injected air bubbles, shows the ramp separation zone to be relatively thin and approximately two-dimensional across the width of the duct. The separated flow region with the natural inlet boundary layer is less than one duct diameter in length.

3.2. Ramp surface pressure distribution

Figures 6 and 7 show the ramp/duct upper centerline surface pressure distribution from the toe of the ramp to the notional pump face with surface arc length, x, for the natural and thickened boundary layer cases, respectively. The break in the distributions is where the dummy pump shaft penetrates the ramp. Of particular interest is the ramp pressure gradient, as this is a major factor affecting ramp separation, and the pressure rise achieved at the last tap (located in the notional pump plane), which affects the pump cavitation number.

The ramp pressure distributions show a monotonic increase in pressure at each tapping with increasing IVR for essentially all but the last tap ahead of the shaft. Here a reduction in pressure at the higher IVR values reflects the separation shown above in Fig. 4. The lack of pressure increase at the tap before the shaft penetration with increasing IVR indicates an ultimate limit on pressure rise before separation occurs. Figures 4 and 5 show that separation occurred for the case of the natural boundary layer at an IVR of 1.75, whereas separation did not occur for an IVR of up to 2 for the thickened boundary layer case. However, the pressure reduction ahead of the shaft penetration for the thickened boundary layer, shown in Fig. 7, suggests that separation might occur at IVR values greater than 2.

The ultimate ramp pressure at the notional pump face rises up to IVR = 1.75 for the natural boundary layer case. In the thickened boundary layer case the pump face pressure rises to an IVR of 2.0 as for the last tapping before the shaft. For the pump plane tap on the duct surface, a slightly higher ultimate pressure rise is achieved with the thickened boundary layer and a greater ramp pressure rise is achieved at the lower IVR values with the natural boundary layer.

For the peripherally averaged static pressures shown in Fig. 20, however, the ultimate pressure rise is always greater for the thickened boundary layer case, except at IVR = 2.0 where the pressure rise for the natural boundary layer becomes equal. The limiting pressure is affected by several factors, but perhaps the most significant is the contraction or thinning of the inlet streamtube with increasing IVR, as shown experimentally by Roberts and Walker (1997) and numerically by Verbeek and Bulten (2001). This contraction acts to minimize the available ingestion area and maximize the internal diffusion within the duct.

Figures 8 and 9 show the effects of the Reynolds number on the pressure distributions with natural and thickened wall boundary layers for an IVR of 1.75. This value was chosen as a trade-off between a practical IVR value and that at which the maximum pressure rise is achieved. The Reynolds number has little effect on

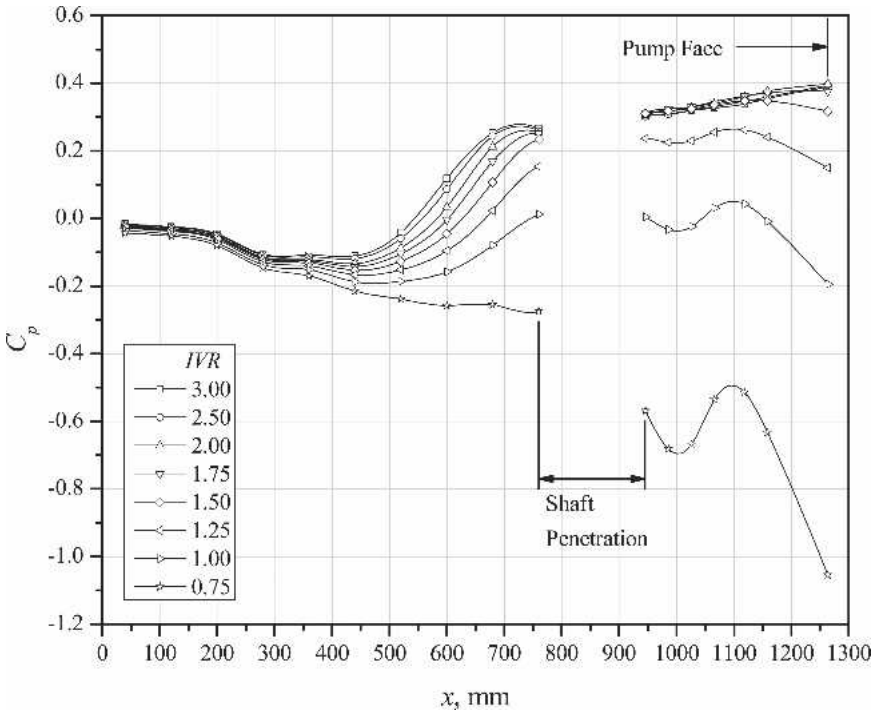

Fig. 6 Ramp pressures with natural wall boundary layer @ $R_{n\infty} = 1 \times 10^6$

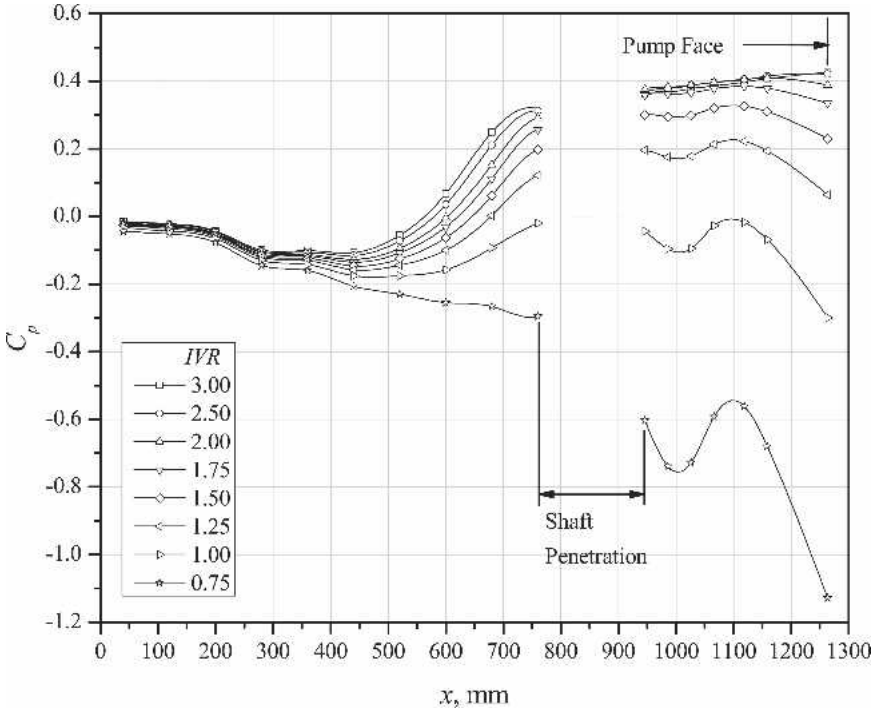

Fig. 7 Ramp pressures with thickened wall boundary layer @ $R_{n\infty} = 1 \times 10^6$

the ramp pressures, except those just ahead and downstream of the shaft for the case of the natural wall boundary layer. A rise in the exit pressures can be seen with increasing Reynolds number, implying that the extent or effect of separation is reduced and may present a lesser issue at full-scale Reynolds numbers (10 to 20 times that of model scale). For the case of the thickened boundary layer, where no separation occurred up to an IVR of 2, there is a lesser Reynolds number dependence.

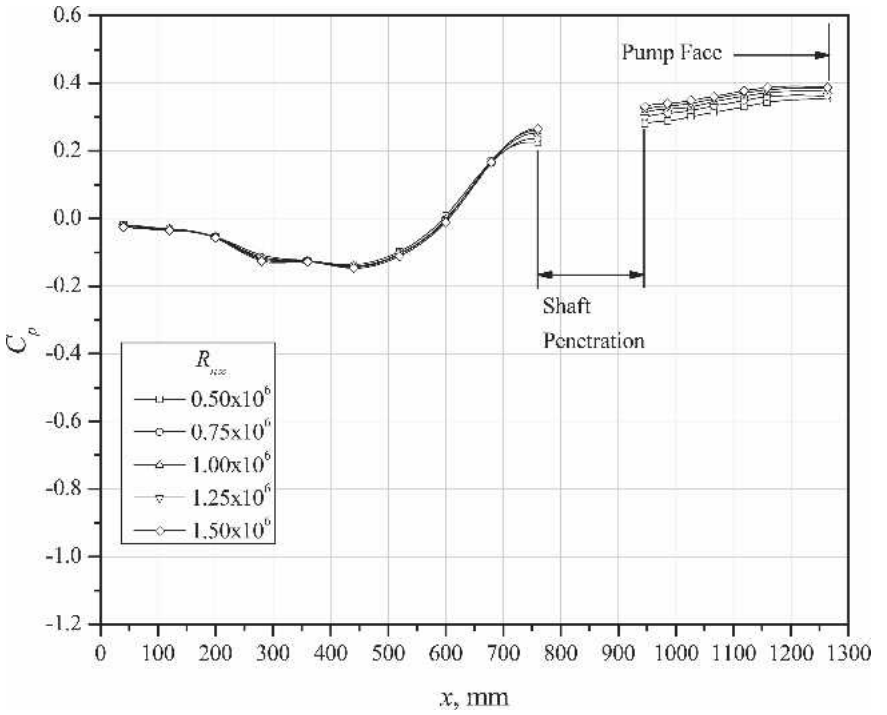

Fig. 8 Ramp pressures with natural wall boundary layer @ IVR = 1.75, effects of changing Reynolds number

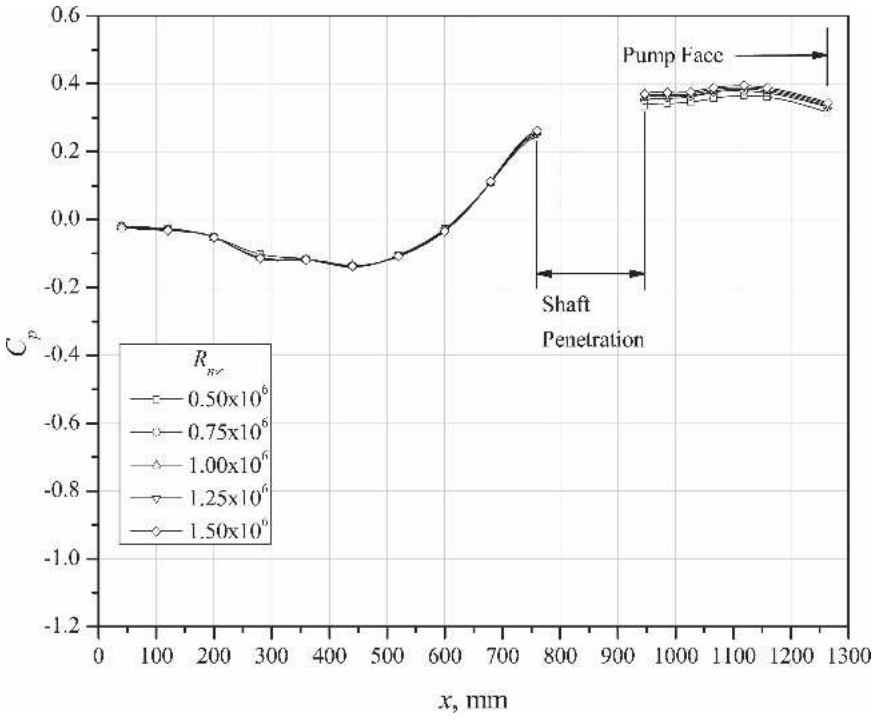

Fig. 9 Ramp pressures with thickened wall boundary layer @ IVR = 1.75, effects of changing Reynolds number

Similar pressure distributions were observed in wind tunnel tests of the same duct geometry (but without a dummy rotor shaft) conducted by Roberts (1998). In that case, the existence of ramp separation at high IVR was confirmed by direct observations of wall shear stress. It is interesting to note that this separation and the associated perturbation of the ramp pressure distribution were not well captured in commercial CFD code predictions reported by both Roberts (1998) and Seil (1998).

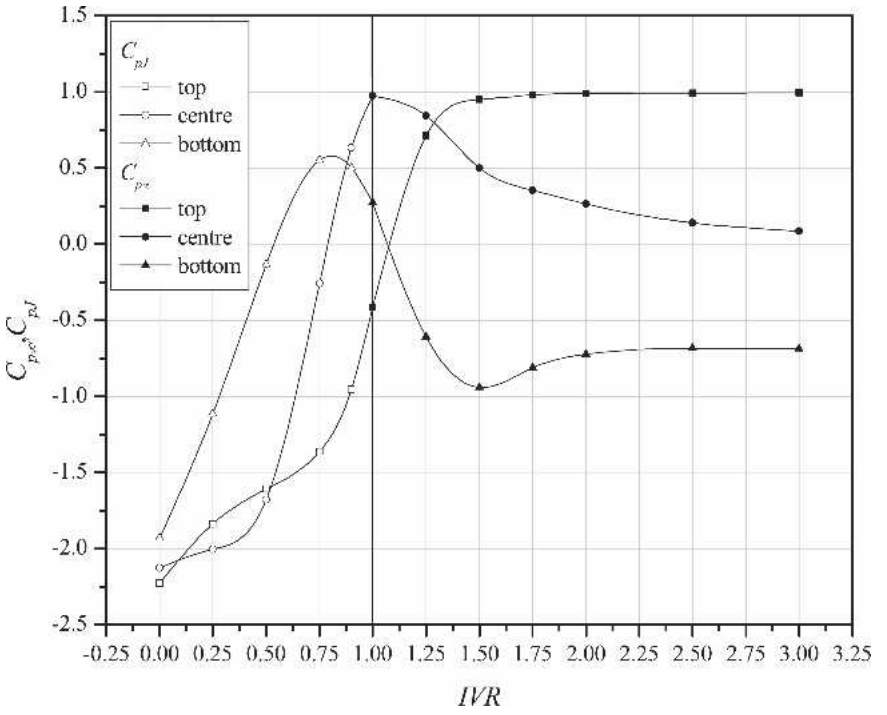

Fig. 10 IVR effects on lip pressures, natural wall boundary layer @ $R_{n\infty} = 1 \times 10^6$

3.3. Lip pressures and incidence

Figures 10 and 11 show the variation of pressure at the three lip tappings with IVR for the natural and thickened boundary layer cases, respectively. Figure 10, for the natural wall boundary layer, shows that ideal incidence (when the center tap pressure reaches a maximum) occurs at an IVR of approximately 1. The maximum value of $C_{p\infty} = 1$ indicates zero energy loss, implying that the stagnation streamline originates from outside the wall boundary layer. The variation in pressure differential between top and bot-

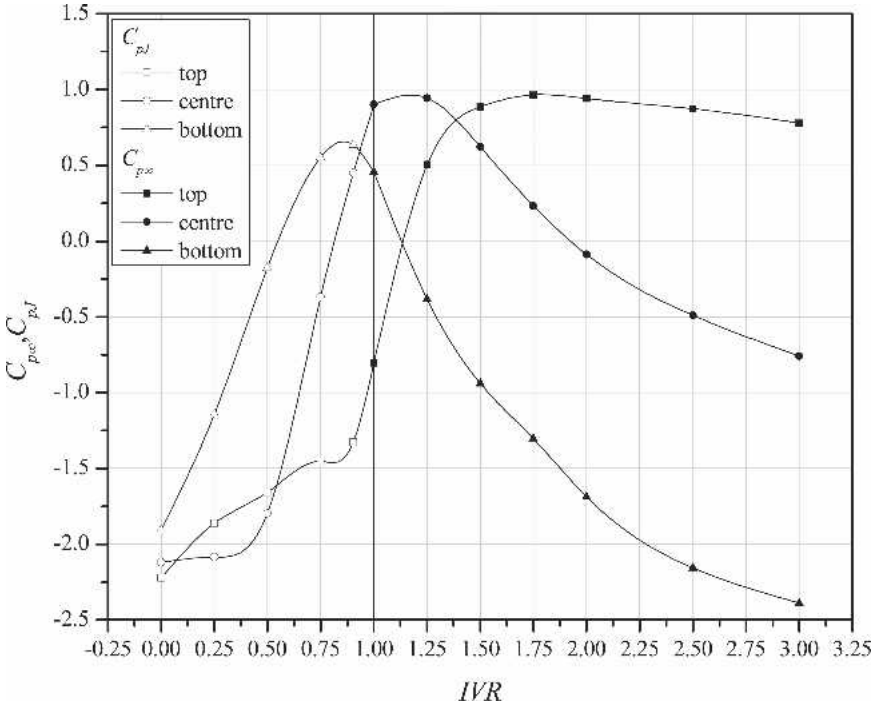

Fig. 11 IVR effects on lip pressures, thickened wall boundary layer @ $R_{n\infty} = 1 \times 10^6$

tom taps indicates the variation of lip incidence (for moderate values of this quantity). With increasing IVR the stagnation streamline moves inside the duct and approaches the lip from above and the pressure is greater at the top tapping. The stagnation point reaches the top tapping (with $C_{p\infty}$ approaching 1) at an IVR of 1.5 and moves further inside the duct at higher IVR, indicating a steady increase in incidence up to about IVR = 2.0. For IVR > 2.0, the lip tapping pressures are approximately constant, suggesting that an ultimate incidence limit has been reached. This asymptotic behavior appears to correlate well with that of the ramp pressures described above, indicating that the pump face pressure recovery and lip incidence are interrelated through the inlet streamtube geometry. For IVR < 1, an opposite change of incidence occurs, with pressure increasing at the bottom tapping. Figure 12 shows the corresponding value of the bottom tapping pressure reaching a maximum around IVR = 0.75; $C_{p\infty} \sim 1$ indicating that the stagnation streamline still originates from outside the boundary layer. Further decrease of the IVR shows a significant drop in pressure for all lip tappings. The limiting incidence at large IVR values reflects the constraints on inflow direction imposed by the duct ceiling and surrounding wall. Far greater incidence changes are possible for IVR values less than the ideal, where the ingestion streamtube is much less confined. It is interesting to note that the ideal incidence occurs at an IVR where the pressure rise at the notional pump face is less than the maximum. This indicates that the test inlet geometry is not optimal and would need modification of the lip geometry to achieve ideal incidence at the IVR for which pump face pressure is a maximum.

Figure 11 shows that ideal incidence for the thickened wall boundary layer occurs at a higher IVR, between 1 and 1.25, compared with 1 for the natural boundary layer. This can largely be attributed to the displacement effect of the thicker boundary layer requiring a thicker inlet streamtube for the same flow rate. As for the natural boundary layer case, the center tap pressure reaches a maximum of $C_{p\infty} = 1$, indicating that the stagnation streamline also originates outside the thickened boundary layer. At IVR values approaching zero the lip pressures for all tappings converge to those of the natural boundary layer case as the influence of the wall boundary layer diminishes. At IVR values greater than that corresponding to ideal incidence, the greater differential between upper and lower lip pressures indicates higher incidence than for the natural boundary layer case. Unlike the case of the natural boundary layer, the lip pressures do not reach limiting values with increasing IVR in the range tested; neither is there a correlation of the lip pressures with those on the ramp and approaching the pump face. This implies that adjustment of the ingestion streamtube continues to a much greater IVR with the thicker boundary layer. While the thicker boundary layer results in a thicker inlet streamtube and hence higher IVR for ideal incidence, it also means greater local flow curvature near the lip at IVR values greater than the ideal. Of particular significance is the much greater incidence tolerance required with a thicker boundary layer.

Figures 12 and 13 show the effect of the Reynolds number on lip pressures for the case of the natural and thickened boundary layers, respectively. The pressure changes are relatively minor at or near stagnation but become greater away from this point particularly for the thickened boundary layer case. This may reflect displacement effects due to local accumulation of low-energy fluid or boundary layer separation on the ramp. This demonstrates that although problems of separation are reduced at higher Reynolds numbers, other problems of lip separation and cavitation may be increased, depending on the IVR.

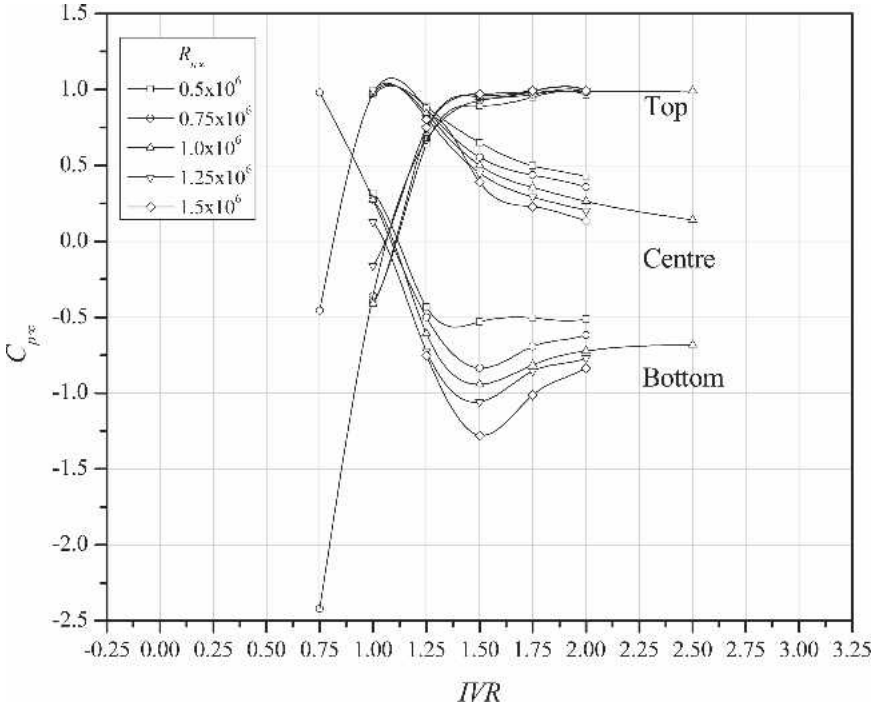

Fig. 12 Reynolds number effects on lip pressures, natural wall boundary layer

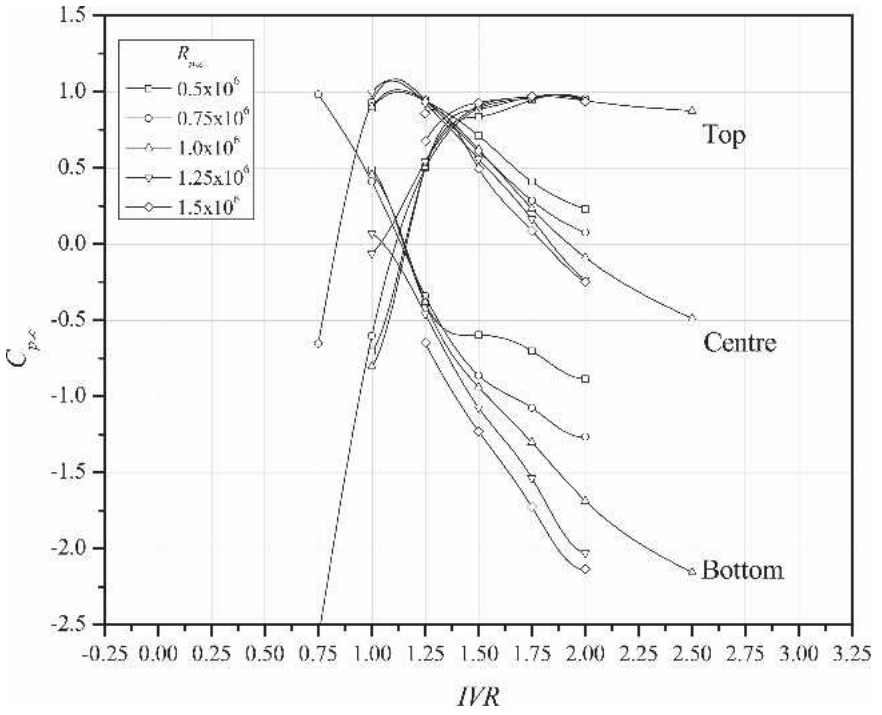

Fig. 13 Reynolds number effects on lip pressures, thickened wall boundary layer

3.4. Pump face flow parameters

Figures 14 and 15 show the pump face total pressure distributions for the natural and thickened boundary layer cases, respectively. In both cases there is a significant total pressure deficit at the top of the disc resulting from the combined effects of the ingested wall boundary layer, the occurrence of ramp separation, the presence of the pump shaft wake, and secondary flow effects within the duct. The magnitude of the deficit is greatest in the case of the natural boundary layer. Here there is a much greater region of total pressure uniformity associated with ingestion of freestream fluid and a sharper energy gradient at its boundary. The energy deficit is greatest at the lowest IVR tested, although it is more locally confined. With increasing IVR the region of deficit expands, with the energy changing more gradually from the top to the bottom of the disc. This is probably due to greater distortion of the inlet streamtube at higher IVR, accompanied by stronger secondary flows associated with the duct curvature and corner flows.

The thickened boundary layer case (Fig. 15) exhibits a wider region of energy deficit due to the smaller area of freestream fluid ingested, and there is a noticeably smoother variation in the total pressure from the top to the bottom of the disc. The general trend of changes in energy distribution with IVR is similar to that for the natural boundary layer. The deficit at the top of the disc is less than that for the natural boundary layer case for all IVR values tested, most likely due to lack of a ramp separation together with reduced secondary flows due to the more uniform inlet velocity distribution. These trends are reflected in the averaged properties presented in Fig. 20, which show that greater flow or area averaged total pressure coefficients are achieved at the pump face in the case of the natural boundary layer for all the IVR values tested. The flow distortion at the pump face, as measured by the DC_{60} parameter, is significantly lower for the thickened boundary layer case.

Figure 21 shows the peripheral variation of static pressure at the notional pump face. For the lowest IVR value, where the mean $C_{p\infty}$ is negative, the variation from the top to the bottom of the disc is approximately 15% of the mean, whereas at the highest IVR values this variation is approximately 5% of the mean. Comparison of Fig. 20 and 21 indicates that a greater static pressure rise is achieved for the natural boundary layer case, up to an IVR value of 2 at which the pressure rise for the thickened boundary layer case becomes equal. As discussed above, the greater pressure rise in the natural boundary layer case produces more adverse ramp pressure gradients and promotes flow separation.

The axial velocity distributions in the plane of the notional pump face shown in Figs. 16 and 17 were estimated from the measured total pressure distributions by assuming a uniform static pressure across the duct equal to the average static pressure on the periphery. This assumption is justified from continuity checks made by comparing the flow rate obtained from integration of the derived velocity distribution with the bulk flow measurement from the electromagnetic flow meter; agreement was generally within a few percent. Velocity distributions on the vertical centerline for a greater range of IVR values have also been derived and are shown in Figs. 22 and 23 for the natural and thickened boundary layer cases, respectively. As expected, these curves reflect the general trends of the total pressure distributions shown in Figs. 14 and 15. For the natural boundary layer case, there is a confined region of velocity deficit at the top of the disc at low IVR values. The deficit becomes greater in magnitude and area with increasing IVR until the velocity varies by more than a factor of 3 from the top to the bottom of the disc at an IVR of 2. For the thickened boundary

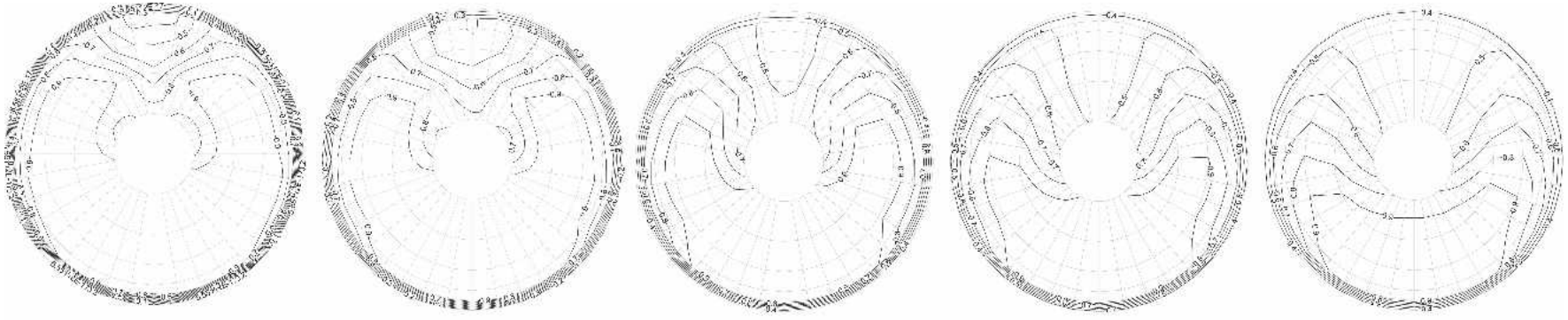

Fig. 14 Pump face total pressure distributions with natural wall boundary layer @ $R_{n\infty} = 1 \times 10^6$, contours of C_P

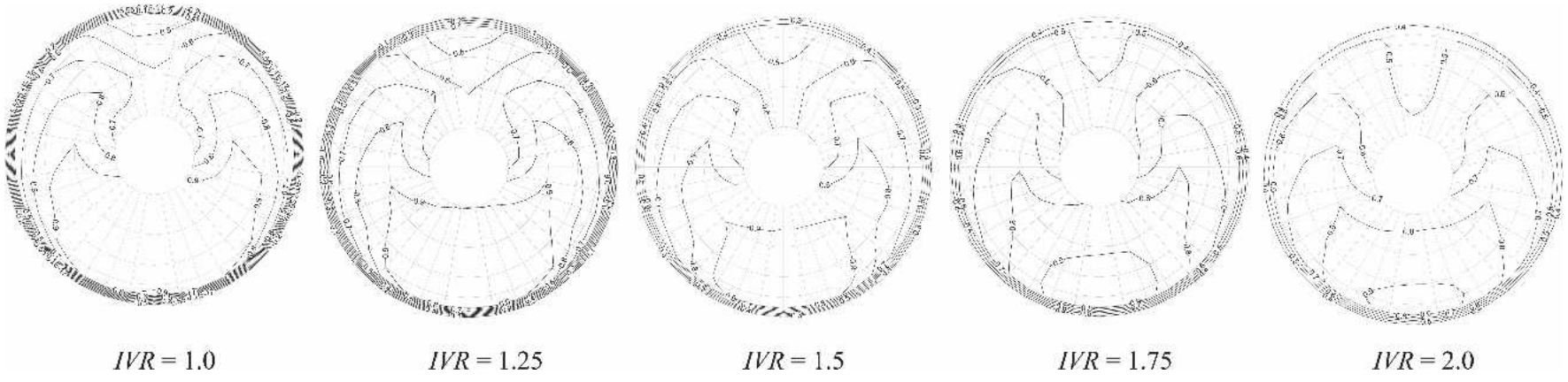

Fig. 15 Pump face total pressure distributions with thickened wall boundary layer @ $R_{n\infty} = 1 \times 10^6$, contours of C_P

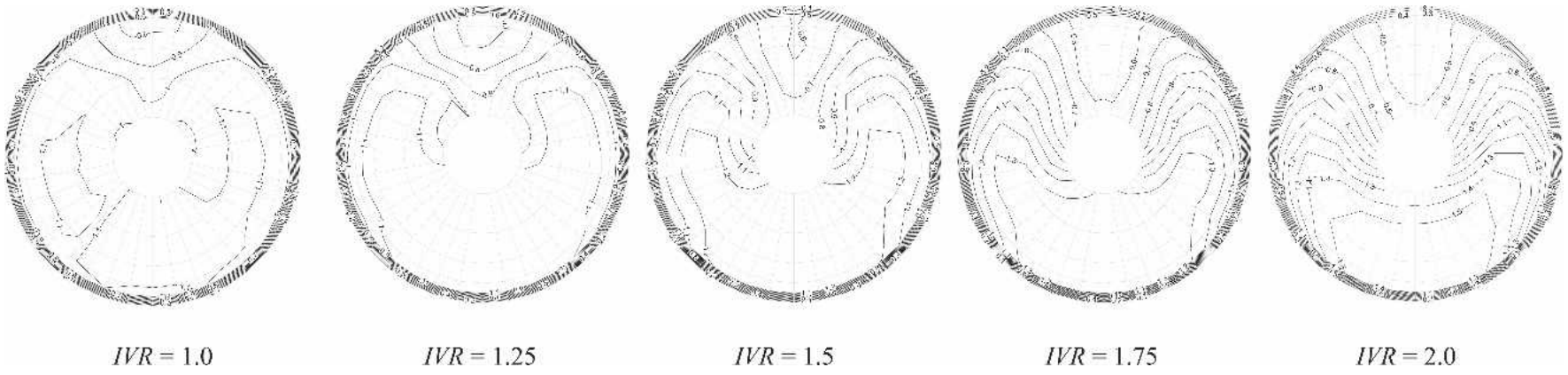

Fig. 16 Pump face axial velocity distributions with natural wall boundary layer @ $R_{n\infty} = 1 \times 10^6$, contours of u/U_J

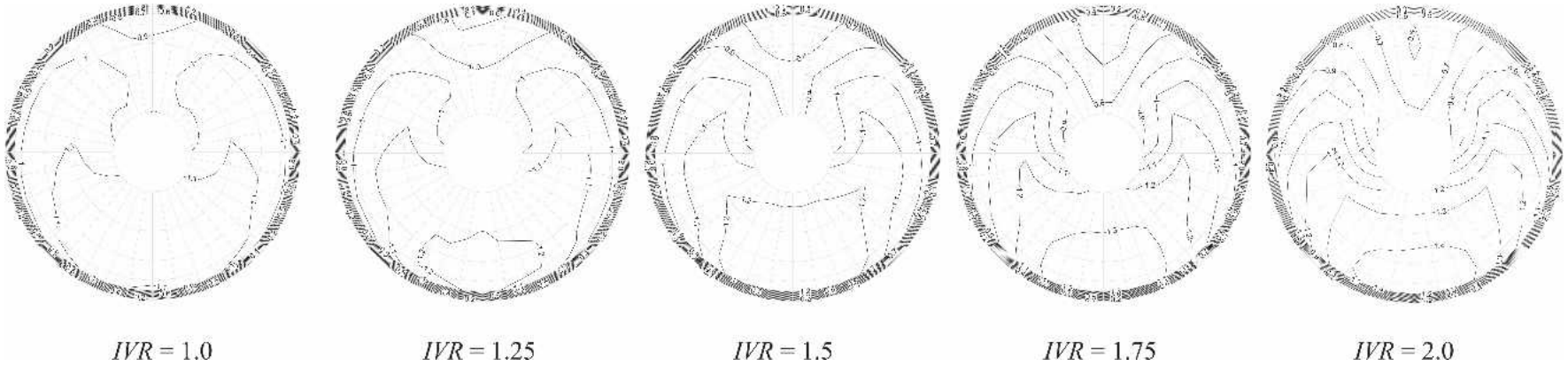

Fig. 17 Pump face axial velocity distributions with thickened wall boundary layer @ $R_{n\infty} = 1 \times 10^6$, contours of u/U_J

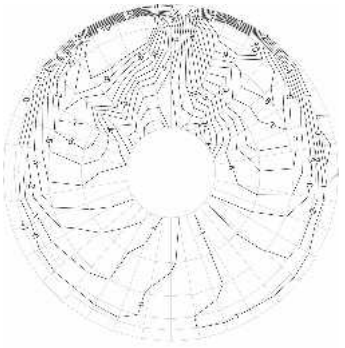

$IVR = 1.75$

Fig. 18 Pump face swirl angle distributions with natural wall boundary layer @ $R_{n\infty} = 1 \times 10^6$, contours of $\alpha = \text{atan}(v/u)°$

layer case, the magnitude of variation from top to bottom is 2.3 and there is a much smoother radial and circumferential variation. Figure 22 shows that optimum uniformity for the natural boundary layer is achieved for IVR ≈ 0.75. For lower IVR values, there is a deficit at the bottom of the disc; for greater values, the deficit occurs at the top of the disc. For IVR > 2, there are negative velocity values, indicating the occurrence of local flow separation. Figure 23 shows that optimum uniformity for the thickened boundary layer also occurs at IVR ≈ 0.75. Comparison of Figs. 22 and 23 again shows the much greater nonuniformity for the natural boundary layer case.

Flow swirl angles were measured with the three-hole pressure probe at selected IVR values (near those at which optimum pressure recovery was achieved) to gain insight into the effects of inlet boundary layer thickness and IVR. Figures 18 and 19 (for the natural and thickened boundary layer cases, respectively) show maximum swirl angles occurring at the top of the disc in all cases, due in large part to the greater axial velocity deficit at the top of the disc. The greatest swirl angles occur for the case of the natural boundary layer with IVR = 1.75, where angles over 10 deg occur. In the case of the thickened boundary layer for the same IVR, the maximum swirl angle reduces to 5 to 6 deg. The greater swirl angles for the natural boundary layer case indicate the presence of stronger secondary flows driven by the higher pressure differentials required to balance the greater inertia forces associated with curvature of the thicker loss-free regions.

Secondary flow in a simple bend causes the high-energy core fluid to move to the outside of the bend. The outer low-energy fluid moves around the circumference to the inside of the bend, and two counterrotating secondary flow structures are created. In the case of a water-jet inlet asymmetric inlet flow associated with hull boundary layer ingestion, together with reversal of longitudinal curvature in the S-shaped duct, further complicate the situation compared with axisymmetric flow entering a simple pipe bend.

Secondary flow due to curvature of the bulk flow is the dominant feature of the present results. Fluid initially moves circumferentially from the bottom of the inlet to the top; continuity requires balancing flows from the top of the inlet to the bottom. The secondary flow is dominated by the initial curvature of the inlet streamtube and ramp, and the developed inertia is such that the following short length of segmented bend of the opposite curvature has little reversing effect. The swirl angle increases significantly as the IVR is raised. At lower IVR values there is a region of counterflow at the sides of the inlet. This counterflowing zone almost vanishes at the highest IVR. Other significant factors include streamwise vortices adjacent to the square corners at the top and bottom of the inlet and the ramp walls, and the shaft wake.

In summary, there are significant differences in the IVR values for optimum pressure recovery, zero lip incidence, and optimum pump face uniformity for the inlet geometry tested. From Figs. 6 and 7, the minimum IVR values to approach maximum pressure recovery at the pump face are 1.75 and 2.0–2.5 for the natural and thickened boundary layer cases, respectively. From Figs. 10 and 11, IVR values for ideal lip incidence are 1.0 and 1.0–1.25 for the natural and thickened boundary layer cases, respectively. Optimum velocity uniformity occurs at an IVR of 0.75 for both inlet boundary layer thicknesses, as shown by Figs. 23 and 24, and velocity uniformity degrades relatively quickly for IVR values above or below this. Zero lip incidence occurs at IVR values quite close to those for favorable uniformity, although both are significantly below IVR values required for acceptable pressure recovery and manageable pump cavitation occurrence. There is a significant all round performance improvement in the case of a thicker inlet

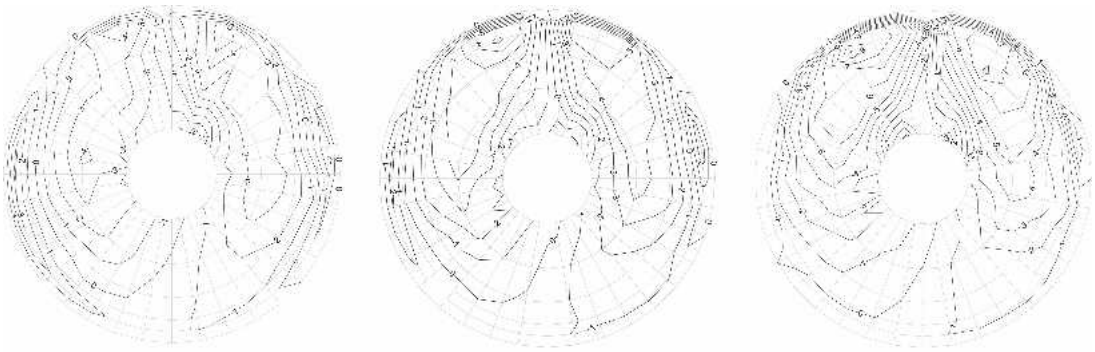

$IVR = 1.5$ $IVR = 1.75$ $IVR = 2.0$

Fig. 19 Pump face swirl angle distributions with thickened wall boundary layer @ $R_{n\infty} = 1 \times 10^6$, contours of $\alpha = \text{atan}(v/u)°$

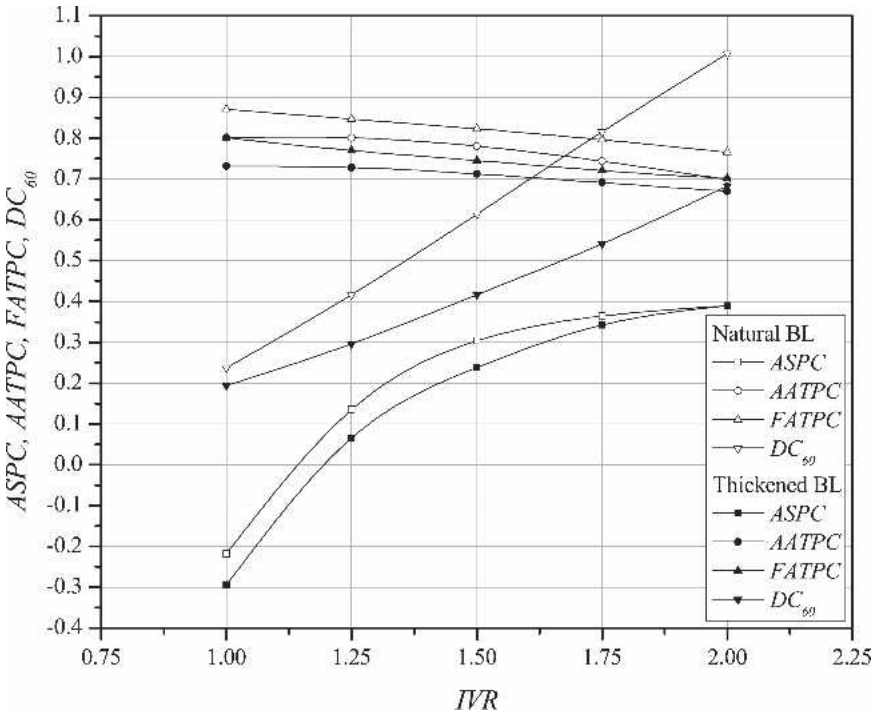

Fig. 20 Pump face averaged total and static pressure and total pressure distortion with natural and thickened boundary layers

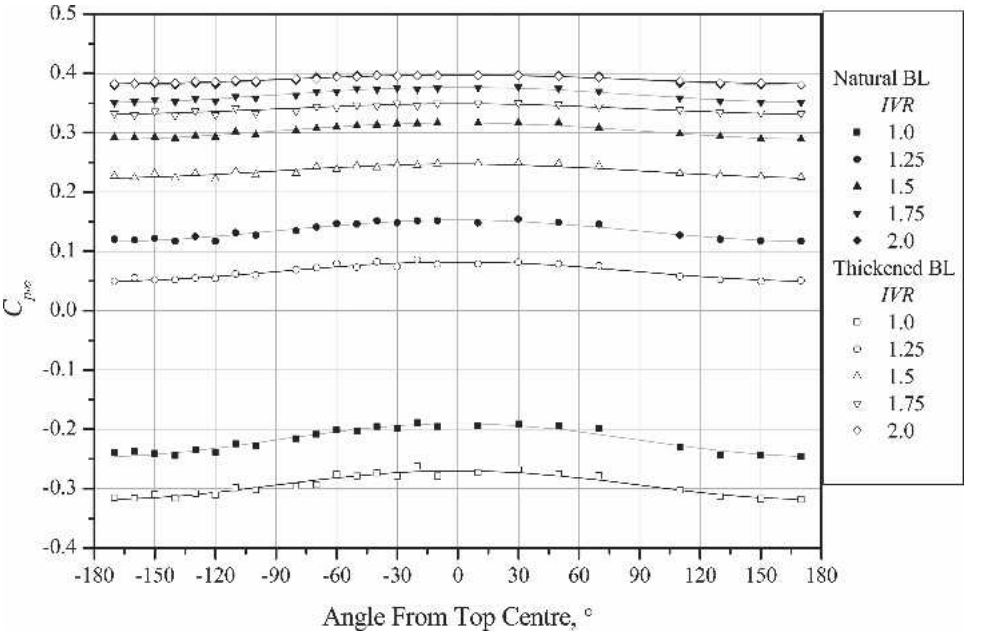

Fig. 21 Pump face wall static pressure distribution with natural and thickened boundary layers

boundary layer; this effect may be even more important at full scale, where the hull boundary layer/duct diameter ratio may exceed that of the present study. These results demonstrate the complexity of the water-jet inlet flow and the scope available for optimization of inlet duct geometry. The inlet geometry tested is clearly not optimal for the current large high-speed craft, which typically cruise with IVR values between 1.5 and 2.3.

3.5. Cavitation inception and occurrence

Water-jet propulsors are invariably used in high-speed applications where freestream cavitation numbers are relatively low, making cavitation difficult to avoid. Besides the pump rotor, the area most susceptible to cavitation is the inlet duct lip, although cavitation may also occur within the duct. Lip cavitation occurs

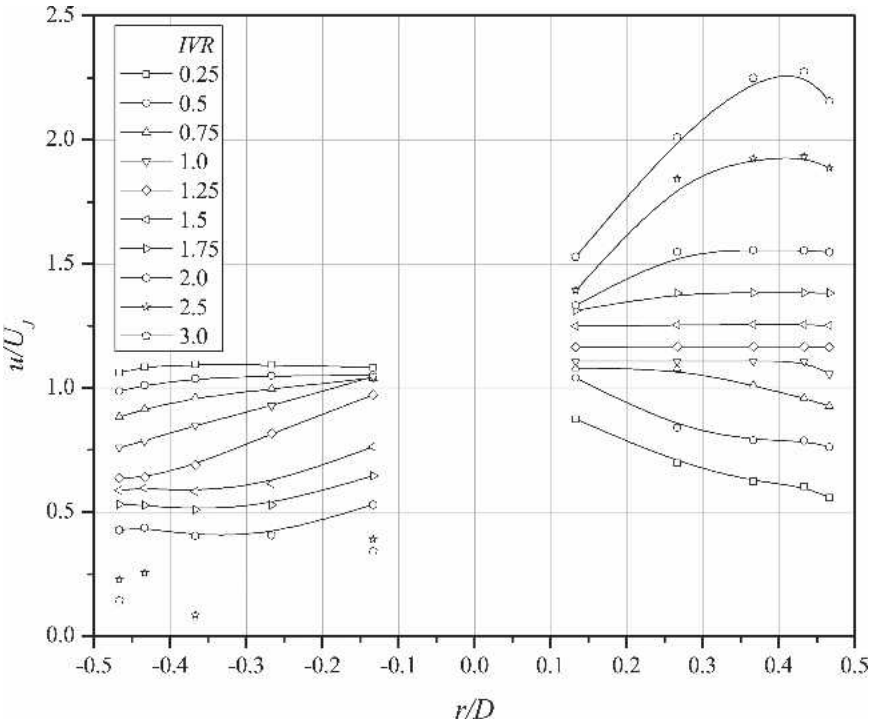

Fig. 22 Pump face vertical distribution of axial velocity for natural boundary layer, effects of changing inlet velocity ratio (IVR)

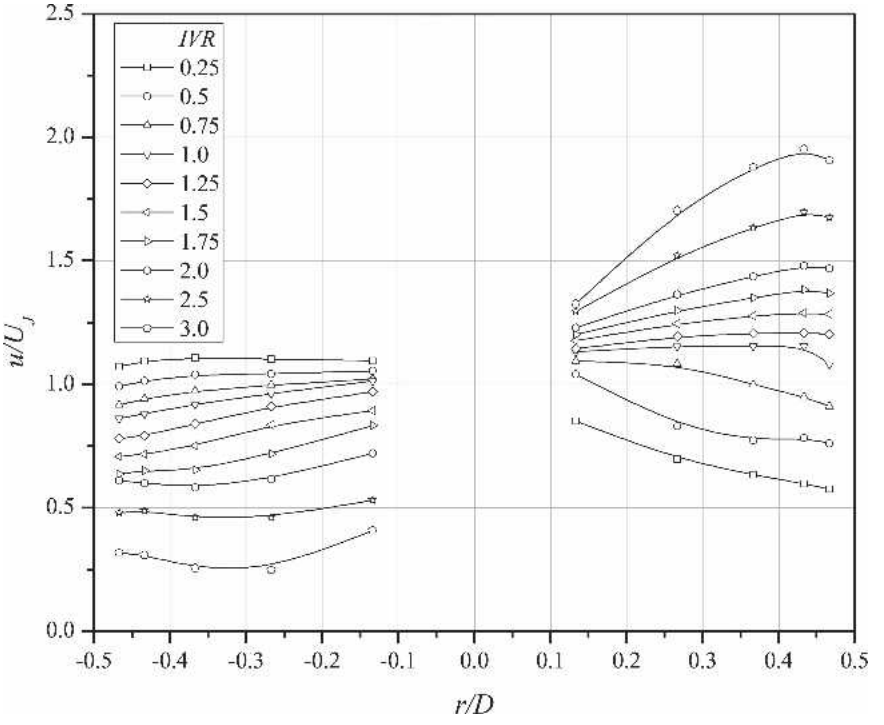

Fig. 23 Pump face vertical distribution of axial velocity for thickened boundary layer, effects of changing inlet velocity ratio (IVR)

due to localized low pressure regions associated with large lip incidence. Figure 24 shows measured lip inception cavitation numbers for the test inlet for a broad range of IVR values and both natural and thickened boundary layer cases. The minima that occur between an IVR of 1 and 1.25 reflect the approach of ideal incidence, corresponding to the stagnation point being located near the lip center, as discussed above. For lower IVR values, cavitation occurs on the inside of the duct; for greater IVR values, it occurs on the outside of the duct lip. The character of lip cavitation is strongly influenced by the magnitude of lip incidence and

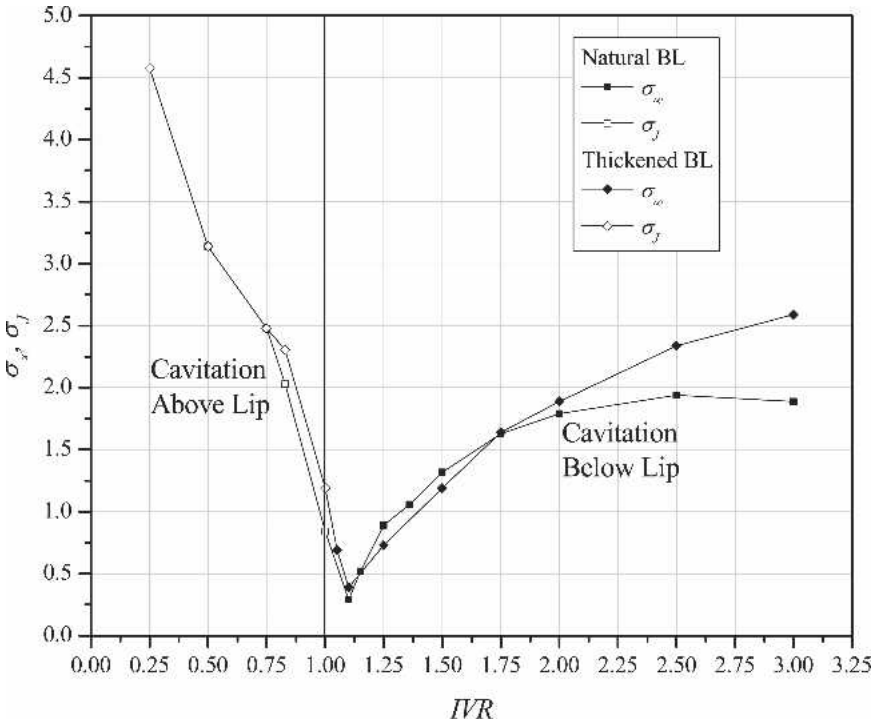

Fig. 24 Lip cavitation inception with natural and thickened boundary layer

the nature of any associated flow separation. Inception occurs at greater cavitation numbers for the natural boundary layer case for $1 < IVR < 1.75$; for $IVR > 1.75$, inception occurs at higher cavitation numbers for the thickened boundary layer case. This corresponds to the behavior of measured pressures on the bottom lip tapping where, for example, the pressure is lower at an IVR of 1.5 for the natural boundary layer case (see Figs. 10 and 11). As discussed above, the lip pressures continue to reduce with increasing IVR in the thickened boundary case and do not reach a limit as in the case of the natural boundary layer; this is reflected in the much greater inception cavitation numbers for $IVR > 1.75$. For the thickened boundary layer case, there is a reasonable correlation between the lip pressures at the bottom tapping and the inception cavitation numbers. For the natural boundary layer case, the correlation exists only for IVR values up to 1.5. Notwithstanding effects of cavitation nuclei strength, this could be attributed to whether cavitation inception occurs near the bottom lip tapping and/or whether inception occurs in the shear layer downstream of the lip associated with flow separation. Similar observations can be made regarding inception on the inside of the duct; however, the correspondence with measured pressures on the center or top lip tappings does not occur, most likely due to inception occurring remote from these tapping positions. For $IVR < 1$, there is a rapid increase in incidence with decreasing IVR, due to the inlet streamtube being less confined. This results in violent bubble or shear layer cavitation occurring, as nuclei are activated and collapse within a narrow region of the separated flow.

Typical geometry and speeds of full-scale high-speed craft result in cavitation numbers at the inlet lip as low as 0.3, indicating that some cavitation may always occur in practice. As operational IVR values are likely to exceed 1.5, the inception cavitation numbers presented in Fig. 24 indicate that relatively large lip cavities can be expected in normal operation. Figures 25 to 29 show examples of lip cavitation for the thickened boundary layer case. Figures 25 to 28 show examples of cavitation occurrence on the outside of the lip. Figure 29 shows an example of cavitation occurrence inside the duct just upstream of the notional pump face. Examples of cavitation occurrence on the inside of the lip are not presented due to the difficulty of manually triggering the photography of these transient cavitation events, for which occasionally captured photographs revealed little detail.

Figures 25 to 27 show cavitation development with decreasing cavitation number beyond inception at an IVR of 1.5. Figure 25 shows a sheet cavity formed from the base of the lip that is associated with a separated region. This cavity exhibits unstable closure, and cavitating vortex filaments are present in the turbulent shear layer further downstream. The extent and shape of the cavity reveal the reattachment of the separated shear layer and outer streamlines downstream of the lip. With further decrease in cavitation number, the cavity grows in both streamwise and transverse extent, as shown in Fig. 26. With increasing cavity length a more coherent closure mechanism develops: there appears to be a reentrant jet combined with perforation toward the cavity leading edge, resulting in the shedding of horseshoe or ring vortices. With reduction of the cavitation number to 0.3 the cavity grows further in both streamwise and transverse directions such that the cavity length becomes comparable to the duct diameter, as shown in Fig. 27: this cavity appears to be globally more stable than that obtained at a cavitation number of 0.6. Cavities of this size and volume would very likely affect the flow within the duct in full-scale applications, particularly if there were unsteadiness due to sea-keeping response. Comparison of Figs. 26 and 27 shows the effect of increasing IVR for the same cavitation number. The cavity grows in base width and length, reflecting the greater extent

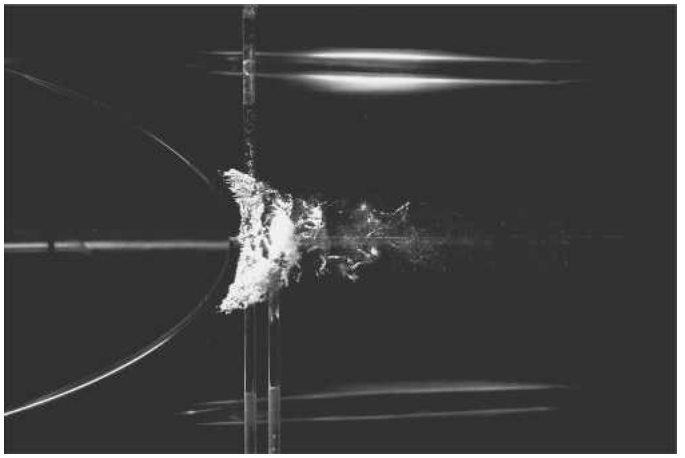

Fig. 25 External lip cavitation with thickened boundary layer, $\sigma_\infty = 1.0$, $R_{n\infty} = 1.0 \times 10^6$, IVR = 1.5

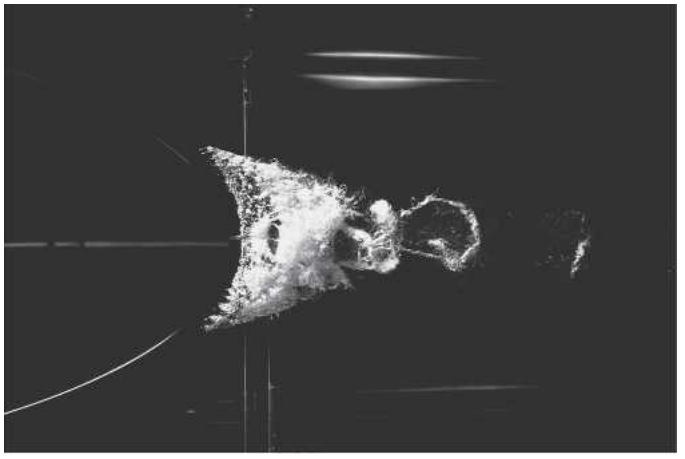

Fig. 26 External lip cavitation with thickened boundary layer, $\sigma_\infty = 0.6$, $R_{n\infty} = 1.5 \times 10^6$, IVR = 1.5

Fig. 27 External lip cavitation with thickened boundary layer, $\sigma_\infty = 0.3$, $R_{n\infty} = 1.5 \times 10^6$, IVR = 1.5

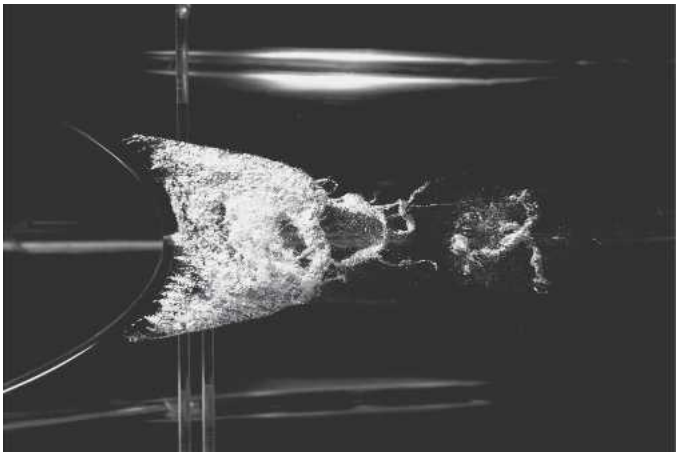

Fig. 28 External lip cavitation with thickened boundary layer, $\sigma_\infty = 0.6$, $R_{n\infty} = 1.0 \times 10^6$, IVR = 1.75

Fig. 29 Duct immediately upstream of notional pump face cavitation with thickened boundary layer, $\sigma_\infty = 0.5$, $R_{n\infty} = 1.25 \times 10^6$, IVR = 1.0 (flow from left to right)

of lip separation with increasing IVR. Cavity closure is again highly unstable with the shedding of large-scale vortical structures.

Cavitation was also observed to occur within the duct at IVR values between 1 and 1.1. The resulting cavities were located at the bottom of the duct, just downstream of the segmented bend or just upstream of the notional pump face. This cavitation appeared as transient, partially isolated, thin bubbles along the wall of the duct, with regions of coalescence, as shown in Fig. 29. The measured pump face velocity distributions indicate this to be a region of high velocity with a relatively thin boundary layer and associated high strain rate. This explains the plate-like nature of the bubble cavities, which may be partly due to the nucleating effect of sheet cavitation occurring on the inside of the lip combined with the perturbation from the segmented bend. These cavities were not observed to occur at lower IVR values, possibly due to a much thicker boundary layer forming from well-developed lip separation. Their absence at higher IVR values can be attributed to the lack of nuclei and/or much lower duct velocities or higher local cavitation numbers.

4. Conclusions

The principal features of flow within a generic flush-type water-jet inlet have been investigated experimentally in a closed-circuit variable-pressure water tunnel. Tests were conducted with natural and thickened tunnel wall boundary layers 13.3% and 30% of inlet duct diameter to simulate the effect of varying vessel hull boundary layer thickness.

Flow separation from the intake ramp just upstream of the pump rotor shaft penetration was observed to occur at IVR = 1.5 for the natural boundary layer case, but was absent up to IVR = 2.0 with the thickened boundary layer. Surface pressure distribution measurements reflected the occurrence of ramp separation at high IVR and revealed an ultimate limit to pressure rise or recovery achievable at the pump face.

The exit pressure was greater for the natural boundary layer case with IVR < 2, and slightly greater for the thickened boundary layer for IVR > 2. The greater pressure rise for the natural boundary layer case at the lower IVR values came at the expense of a more adverse ramp pressure gradient and consequent earlier ramp separation. The thickened inlet boundary layer reduced the strength of secondary flow within the duct and resulted in lower distortion of the exit total pressure and velocity distributions up to IVR = 2.

Measured lip pressures indicated the stagnation streamline to originate from within the freestream for both the natural and thickened boundary layer cases. Ideal lip incidence occurred at IVR values (between 0.75 and 1.25) quite close to those for favorable uniformity of pump face flow parameters, but significantly below the IVR range (between 1.75 and 2.5) required for acceptable pressure recovery and manageable pump cavitation occurrence. This indicates that the test inlet geometry was not optimal and would require modification to achieve satisfactory operation for modern large high-speed craft with typical operational cruise values of IVR between 1.5 and 2.25.

Observations of cavitation inception suggested that cavitation of flush inlets in full-scale vessel operation is likely to occur for all operating conditions through maneuvering, cruise, and lightship cruise. The test inlet exhibited the development of large cavities with both steady and unsteady closure. The large cavity volumes observed have the potential to further increase bulk inlet flow unsteadiness for a vessel operating in a seaway, due to the additional pressure fluctuations imposed by surface waves.

The test results have improved understanding of the basic flow phenomena in flush-type inlets for water-jet propulsion systems, and provided valuable data for CFD code validation studies and future inlet design optimization.

Once validated for typical inlet geometries and operating conditions, CFD predictions are likely to provide a fairly reliable guide to the effects of moderate changes in geometry or off-design operation. In particular, CFD analyses should provide useful guidance as to the effects of inlet flow unsteadiness due to wave or vessel motions, and to the effects of inlet yaw due to upstream hull asymmetry or the effects of turning maneuvers.

Acknowledgment

The authors wish to acknowledge the support of the Australian Maritime College, the University of Tasmania, and the assistance of Mr. Robert Wrigley and Mr. David Clarke in carrying out the experiments.

References

ALLISON, J. 1993 Marine water-jet propulsion, *Transactions of the Society of Naval Architects and Marine Engineers,* **101,** 275–335.

BRANDNER, P. A., AND WALKER, G. J. 2001 A waterjet test loop for the Tom Fink Cavitation Tunnel, *Proceedings,* Waterjet Propulsion Conference III, RINA, February 20, Gothenburg, Sweden, paper no. 1, 11 pp.

BRANDNER, P. A., CLARKE, D. B., AND WALKER, G. J. 2004 Development of a fast response probe for use in a cavitation tunnel, *Proceedings,* 15th AFMC, December, Sydney, Australia, paper no. AFMC 00195, 4 pp, on CD.

Fast Ferry International. 2001 Database on CD.

RINA. 1994 *Proceedings,* International Conference on Waterjet Propulsion I, Royal Institution of Naval Architects, London.

RINA. 1998 *Proceedings,* International Conference on Waterjet Propulsion II, Royal Institution of Naval Architects, Amsterdam.

RINA. 2001 *Proceedings,* International Conference on Waterjet Propulsion III, Royal Institution of Naval Architects, Gothenburg.

RINA. 2004 *Proceedings,* International Conference on Waterjet Propulsion IV, Royal Institution of Naval Architects, London.

ROBERTS, J. L., 1998 *The Influence of Hull Boundary Layers on Waterjet Intake Performance,* Ph.D. thesis, University of Tasmania.

ROBERTS, J. L., AND WALKER, G. J. 1997 Bounding ingestion streamtube determination via a CO tracer, *Experiments in Fluids,* **24,** 5/6, 518–520.

SARGISON, J. E., WALKER, G. J., BOND, V., AND CHEVALIER, G. 2004 Experimental review of devices to artificially thicken wind tunnel boundary layers, *Proceedings,* 15th AFMC, December, Sydney, Australia, paper no. AFMC 00091, 4 pp. on CD.

SEIL, G. J. 1998 *Computational Fluid Dynamics Investigation and Opimisation of Waterjet Propulsion Unit Inlet Design,* Ph.D. thesis, Department of Mechanical and Manufacturing Engineering, University of New South Wales.

VERBEEK, R., AND BULTEN, N. W. H. 2001 Interpretation of model scale results with the aid of CFD calculations, Proceedings, International Conference on Waterjet Propulsion III, RINA, Gothenburg, Sweden, paper no. 6, 9 pp.

Appendix A

Blockage correction (one-dimensional)

Due to extraction of jet flow, the velocity at the entrance and exit of the test section will be different, and some corrections to measured parameters are desirable to better reflect the values that would be obtained with the inlet operating in an infinite flow domain. Assuming the effective freestream velocity U_∞ in the neighborhood of the inlet to be the mean of values at the test section inlet and exit gives, from continuity:

$$U_\infty = U_{ref} - \frac{U_J A_J}{2A_{ref}} \tag{A1}$$

where U_{ref} and A_{ref} are the measured test section velocity and area at the reference position upstream of the inlet.

Applying the Bernoulli equation between the reference position and the location where the effective freestream velocity U_∞ is achieved gives

$$\frac{p_{ref} - p_\infty}{1/2\rho U_{ref}^2} = \left(\frac{U_\infty}{U_{ref}}\right)^2 - 1 \tag{A2}$$

where p_{ref} is the static pressure at the test section reference position.

Using equation (A1), the effective IVR corrected for blockage effects is given by

$$\mathrm{IVR} = \frac{U_\infty}{U_J} = \frac{U_{ref}}{U_J} - \frac{A_J}{2A_{ref}} \tag{A3}$$

The measured static pressure coefficient,

$$C_{pm} = \frac{p - p_{ref}}{1/2\rho U_{ref}^2} \tag{A4}$$

may be corrected by combining equations (A3) and (A4) to give

$$C_p = \frac{p - p_\infty}{1/2\rho U_\infty^2} = (C_{pm} - 1)\left(\frac{U_{ref}}{U_\infty}\right)^2 + 1 \tag{A5}$$

where from equation (A1)

$$\frac{U_{ref}}{U_\infty} = 1 + \frac{1}{2\text{IVR}}\frac{A_J}{A_{ref}} \tag{A6}$$

The total pressure coefficients may be similarly corrected. Likewise the measured cavitation number, σ_m, may be corrected. The effective cavitation number is given by

$$\sigma = \frac{p_\infty - p_v}{1/2\rho U_\infty^2} = (\sigma_m + 1)\left(\frac{U_{ref}}{U_\infty}\right)^2 - 1 \tag{A7}$$

where

$$\sigma_m = \frac{p_{ref} - p_v}{1/2\rho U_{ref}^2} \tag{A8}$$

is the measured cavitation number.

For a typical IVR of 2 and $R_{n\infty} = 1 \times 10^6$, the loop and test section mean velocities were about 3.5 and 7 m/s, respectively. This gives a loop flow rate about 2.5% of the test section flow, with corresponding corrections of approximately 1% to the IVR and 2.5% to the measured pressure coefficients and cavitation numbers. Under these circumstances, a simple first-order blockage correction based on the preceding one-dimensional flow model is considered adequate.

Appendix B

Details of water-jet test loop

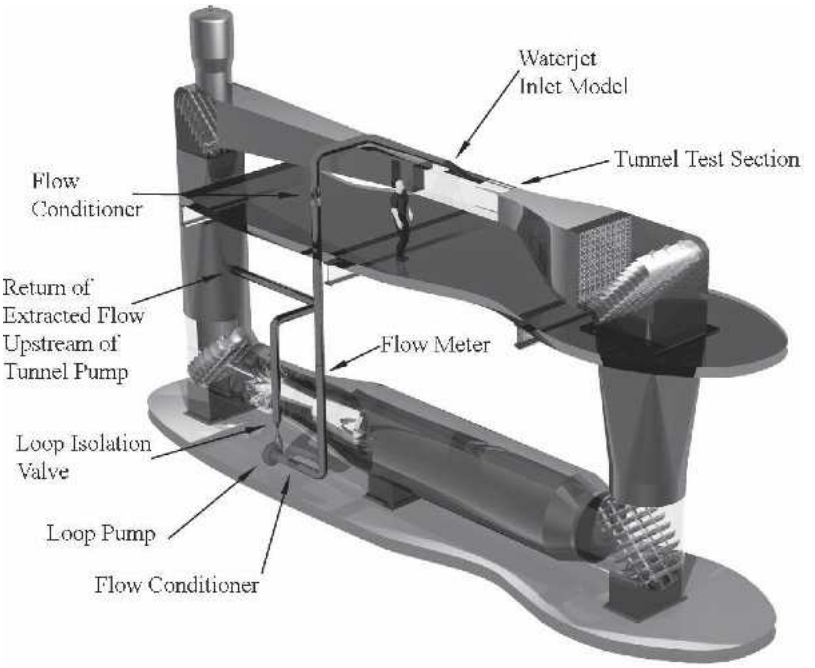

Tunnel particulars	
Test section length	2.6 m
Test section cross section (entry)	0.6 m wide × 0.6 m deep
Test section cross section (exit)	0.6 m wide × 0.62 m deep
Maximum velocity	12 m/s
Velocity spatial nonuniformity	<±1% mean velocity
Velocity temporal variation	<1% mean velocity
Maximum/minimum pressure	4.0/0.04 atmosphere absolute
Temporal stability of pressure	<±0.004 atmosphere absolute
Maximum/minimum cavitation number	5.5/0.2
Water-jet test loop particulars	
Maximum water-jet diameter	150 mm
Maximum flow rate	150 l/s
Flow measurement	Magnetic flowmeter <0.5% accuracy
Flow control	Closed loop flow feedback
Flow temporal variation	<1% flow
Pump motor	AC variable speed 37 kW